RSC Advances

ROYAL SOCIETY OF CHEMISTRY

PAPER

View Article Online
View Journal | View Issue

Cite this: *RSC Adv.*, 2020, **10**, 8821

CO_2 photoreduction to CO/CH_4 over $Bi_2W_{0.5}Mo_{0.5}O_6$ solid solution nanotubes under visible light

Yang Wang,[a] Jiaxu Liu,[a] Ye Wang[a] and Mingyi Zhang *[ab]

In this work, $Bi_2W_{0.5}Mo_{0.5}O_6$ solid solution nanotubes have been synthesized through a structure-directing hard template approach, which demonstrated greatly enhanced CO_2 photoreduction to CO/CH_4. The crystalline phase, components and morphologies of the as-prepared composites were investigated by X-ray diffraction (XRD), scanning electron microscopy (SEM) and transmission electron microscopy (TEM). The present design of $Bi_2W_{0.5}Mo_{0.5}O_6$ solid solution nanotubes leads to remarkably enhanced photocatalytic activities with a peak CO/CH_4 production rate of 6.55/3.75 mmol g^{-1} h^{-1} under visible light irradiation at room temperature, which was about 7 times that on pure Bi_2WO_6 and Bi_2MoO_6 nanotubes, respectively. Hollow nanotubular structures and synergistic electronic effects of various elements contribute to the enhanced visible light photocatalytic activity of $Bi_2W_{0.5}Mo_{0.5}O_6$ solid solution nanotubes.

Received 21st January 2020
Accepted 20th February 2020

DOI: 10.1039/d0ra00672f

rsc.li/rsc-advances

1. Introduction

As a major greenhouse gas causing global warming, the carbon dioxide (CO_2) level in the atmosphere has been increasing steadily over the past centuries as a result of human activities, and therefore the fixation and conversion of CO_2 into C1/C2 energy compounds (such as CO, CH_4, CH_3OH, and/or C_2H_5OH) is an increasingly important issue, and it holds the promise of solving both energy and environmental problems.[1–4]

Oxide semiconductors with Aurivillius structures are of immense importance due to their layered structures and unique properties.[5–16] Among these semiconductors, Bi_2WO_6 is significant because of its excellent intrinsic physico-chemical properties. In order to further improve the utilization of visible light, Bi_2WO_6-based heterojunction composites have been developed.[17–23] Among the strategies to improve the photocatalytic efficiency of Bi_2WO_6, it is an effective method to construct the solid solution photocatalyst. Based on the above consideration, the construction of $Bi_2Mo_xW_{1-x}O_6$ solid solutions attracts our interest in particular because of their structural analogy. That is, (1) Bi_2MoO_6 has a similar Aurivillius layered structure to that of Bi_2WO_6. Compared with Bi_2WO_6, Bi_2MoO_6 with a narrower band gap has the ability to harness more sunlight. (2) The W component can endow the material with high photocatalytic activity, whereas the Mo constituent contributes to the narrow band gap, it is reasonable to postulate that the $Bi_2Mo_xW_{1-x}O_6$ solid solutions may provide a suitable option.

In addition, many works show that the hollow structure has many useful functions: (1) the hollow structure is conducive to the rapid transfer of substances in its internal space; (2) to make its high surface volume ratio to absorb a large number of chemical substances; (3) the unique structure can make light in its internal space for multiple reflections, thus improving the utilization rate of light. To the best of our knowledge, the fabrication and photocatalytic property of tubes-structured $Bi_2Mo_xW_{1-x}O_6$ solid solutions has not yet been reported.

In this paper, we report the synthesis of the $Bi_2Mo_{0.5}W_{0.5}O_6$ solid solution nanotubes using PAN nanofibers as the hard template through solvothermal method. Photocatalytic experiments showed that, compared with Bi_2MoO_6 and Bi_2WO_6 nanotubes, the $Bi_2Mo_{0.5}W_{0.5}O_6$ solid solution nanotubes exhibited excellent photocatalytic activity, which significantly improved the catalytic activity of CO_2 photoreduction.

2. Experimental section

2.1. Fabrication of polyacrylonitrile (PAN) nanofibers

Electrospun polyacrylonitrile nanofibers were fabricated as previously reported.[24] In a typical procedure, 3 g of polyacrylonitrile (PAN) (M_w *ca.* 60 000) powders were dissolved in 20 mL of *N*,*N*-dimethylformamide (DMF) solution. After stirring at room temperature for 15 hours to form a uniform solution, the precursor solution was pumped into a hypodermic syringe for electrospinning. A piece of copper pin connected to a high voltage generator was put into the solution. The positive voltage applied to the tip was 10 kV and the distance between the needle

---

[a] *Key Laboratory for Photonic and Electronic Bandgap Materials, Ministry of Education, School of Physics and Electronic Engineering, Harbin Normal University, Harbin 150025, PR China. E-mail: zhangmingyi@hrbnu.edu.cn; mysci@foxmail.com*

[b] *School of Materials Science and Engineering, Zhengzhou University, Zhengzhou, 45001, PR China*

tip and the collector was 12 cm. The spinning PAN nanofibers are collected on the aluminum foil.

2.2. Fabrication of $Bi_2Mo_{0.5}W_{0.5}O_6$ solid solution nanotubes

In a typical case, 0.125 mmol $Na_2MoO_4\cdot 2H_2O$, 0.125 mmol $Na_2WO_4\cdot 2H_2O$ and 0.5 mmol $Bi(NO_3)_3\cdot 5H_2O$, were dissolved in 40 mL of ethylene glycol (EG) under magnetic stirring for 10 min. The resulting transparent solution was transferred to a 50 mL teflon-lined stainless steel autoclave and PAN nanofibers (15 mg) were added. The autoclave is then heated to 160 °C and maintained for 24 hours. The obtained polyacrylonitrile/$Bi_2W_{0.5}Mo_{0.5}O_6$ hybrid nanofibers were washed with deionized water and ethanol to remove any ionic residual. And, it was denoted as PAN/BWMO. By heating the obtained PAN/BWMO hybrid nanofibers in oven at 500 °C at a ramp rate of 2 °C min^{-1} and maintained for 2 h, the $Bi_2W_{0.5}Mo_{0.5}O_6$ solid solution nanotubes (named as BWMO NTs) were prepared. For comparison, Bi_2MoO_6 and Bi_2WO_6 nanotubes were also synthesized through this method ($Na_2WO_4\cdot 2H_2O$ or $Na_2MoO_4\cdot 2H_2O$ just choose one) and were denoted as BWO NTs and BMO NTs.

2.3. Characterization

The phase purity of the products was characterized by X-ray diffraction (XRD; D/max2600, Rigaku, Japan). Field emission scanning electron microscope (FESEM) images were performed using a SU70 microscope (Hitachi, Japan). Transmission electron microscopy (TEM) images were obtained on a JEOL JEM-2010 instrument. An energy dispersive X-ray (EDX) spectroscope coupled to a TEM was used to analyze the composition of the samples. The UV-Vis diffuse reflectance (DR) spectroscopy of the samples was recorded on a Cary 500 UV-Vis-NIR spectrophotometer.

2.4. Photocatalytic test

The photocatalytic CO_2 reduction experiment was conducted under 300 W xenon lamp. Quartz plates are provided on the top of the airtight reactor and sampling ports are provided on both sides, with a volume of 500 mL. In a typical process, 0.1 g catalyst was uniformly dispersed onto the watch-glass with an area of $\sim$20 cm^2, which then put in the reactor cell. After that, the photocatalysts was sealed in the reactor. Before the irradiation, high purity CO_2 was bubbled through deionized water and then flowed into the reactor for 30 min to remove the residual air. During irradiation, 2 mL gas was taken from the reactor at regular intervals (1 h) for subsequent gas concentration analysis using a gas chromatograph (Agilent 7890A GC) equipped with a flame ionized detector (FID) and methanizer. The produced gases were calibrated with a standard gas mixture and their identity determined using the retention time.

3. Results and discussions

The SEM images (Fig. 1a) reveal that all the as-electrospun PAN nanofibers with diameters of 150–200 nm has a smooth surface without secondary structure. After solvothermal treatment, the $Bi_2W_{0.5}Mo_{0.5}O_6$ solid solution with high coverage density is vertically grown on the PAN nanofibers surfaces, indicating the formation of polyacrylonitrile/$Bi_2W_{0.5}Mo_{0.5}O_6$ hybrid nanofibers (Fig. 1b). Through heat treatment of the as-prepared PAN/BWMO hybrid nanofibers to remove the PAN core, $Bi_2W_{0.5}Mo_{0.5}O_6$ solid solution with tubes-structured are obtained. From the Fig. 1c, we can see that the outer diameter of the BWMO NTs channel is estimated at 400 nm, the wall thickness is estimated at around 80 nm, and the average diameter of the BWMO NTs channel is estimated at 240 nm. From the TEM images (Fig. 1d), A clear contrast between the dark edges and the pale center can be observed, this further confirms that the BWMO NTs have a hollow interior.

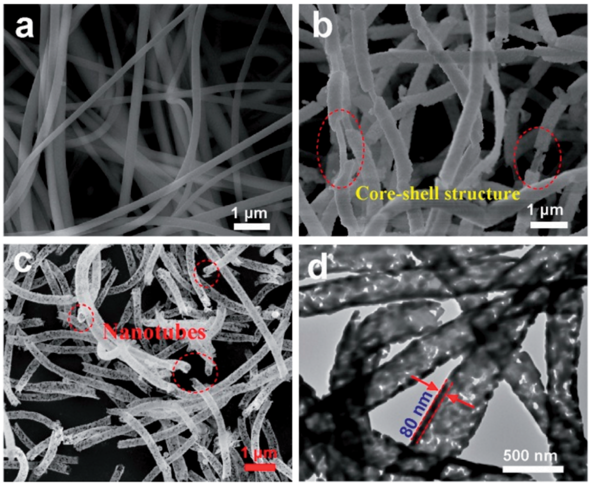

Fig. 1 (a) SEM image of PAN nanofibers. (b) SEM image of the PAN/BWMO nanofibers. (c) SEM image of the BWMO NTs. (d) TEM image of the BWMO NTs.

In order to further clarify the composition distribution and structural characteristics of the product, TEM-EDX scanning along the BWMO NTs radial direction (red line in the inset of Fig. 2) was used to obtain the spatial distribution of the components of the nanotube structure. Three signal peaks for Bi, W and Mo is found in the wall region. This is consistent with the BWMO NTs configuration observed in the SEM and TEM image. In addition, EDX analysis indicates that the molar ratio of W and Mo is about 1 : 1.05 for the BWMO NTs.

From the XRD patterns (Fig. 3), we can see that the PAN nanofibers are poorly crystallized. As aforementioned, Bi_2MoO_6 and Bi_2WO_6 are Aurivillius structures so they have same crystal structure in the normal conditions. Therefore, XRD spectra cannot be utilized to distinguish between these two Aurivillius structures since their peaks are obtained at almost the same diffraction angles. As for the pattern of PAN/BWMO hybrid nanofibers, some strong diffraction peaks can be perfectly indexed to Bi_2MoO_6 or Bi_2WO_6 (JCPDS 76-2388), indicate the formation of $Bi_2W_{0.5}Mo_{0.5}O_6$ solid solution. The XRD pattern of the BWMO NTs shows higher intensity and narrower diffraction peaks, implying the leading role of calcination in the enhancement of crystallization.

Fig. 4 displays the UV-Vis diffuse reflectance (DR) spectroscopy of the PAN nanofibers, PAN-BWMO and the BWMO-NTs.

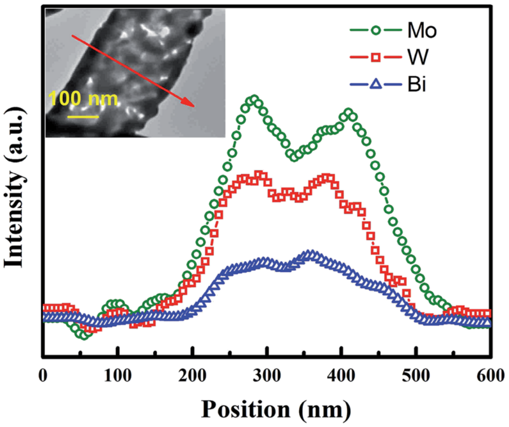

Fig. 2 TEM-EDX line scans spectra of BWMO NTs.

As observed in Fig. 4 there was no peak of PAN nanofibers, while PAN-BWMO and the BWMO-NTs shows a major absorption band between 370 nm and 510 nm. The steep shape of the absorption edge indicates a band-gap transition rather than the transition from the impurity level. For a crystalline semiconductor, the optical absorption near the band edge follows the equation $\alpha h\nu = A(h\nu - E_g)^{n/2}$, where, α, ν, E_g and A are the absorption coefficient, the light frequency, the band gap and a constant, respectively. Among them, n decides the characteristics of the transition in a semiconductor. In this paper, the band gap of BWMO-NTs is calculated as approximately 2.59 eV starting from the absorption edge (inset of Fig. 4), indicating that BWMO-NTs has a suitable band gap for photocatalytic reactions under visible-light irradiation.

As discussed above, the as-prepared BWMO-NTs exhibit one dimensional hollow structure with large surface area, rendering it an excellent candidate for photocatalytic CO_2 reduction. The photocatalytic performance of BWMO-NTs photocatalysts was evaluated and compared to that of pure BWO NTs and pure BMO NTs under visible light irradiation. Control experiments showed no CH_4 or CO production in the absence of either catalyst or irradiation, implying that both catalyst and irradiation are necessary for the present gaseous CO_2 photoreduction system (no show). The primary results showed CO_2 can be reduced to CO and CH_4 in the presence of H_2O vapor and the BWMO NTs, and no other reduced product such as CH_3OH, HCHO or HCOOH is detected. In addition, when N_2 is used to replace CO_2 in the photoreaction system, neither CO/CH_4 nor other carbon-based organic compounds can be detected, indicating that the formation of CO/CH_4 is caused by the CO_2 photoreduction process on the catalyst.

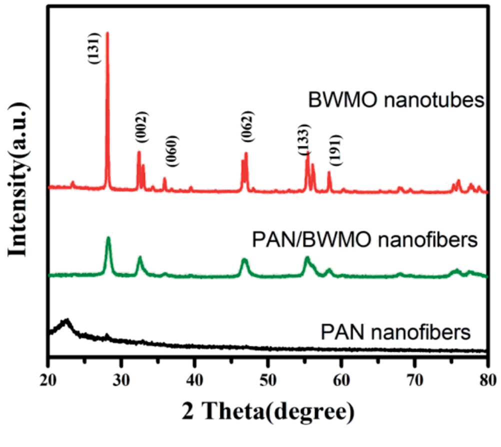

Fig. 3 XRD patterns of the samples.

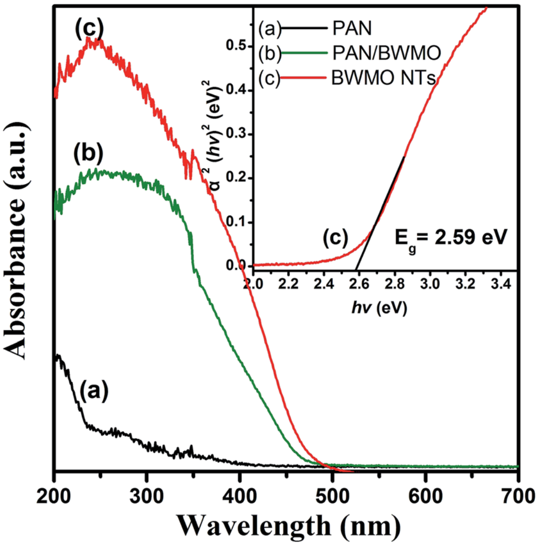

Fig. 4 UV-Vis diffuse reflectance spectra of PAN nanofibers (curve a), PAN-BWMO (curve b) and BWMO-NTs (curve c).

As shown in Fig. 5a–c, under visible light irradiation, CO_2 can be reduced to CH_4 and CO in the presence of water vapor by using the $Bi_2W_{0.5}Mo_{0.5}O_6$ solid solution as the photocatalysts. The pure BWO NTs show poor CO and CH_4 production (0.93

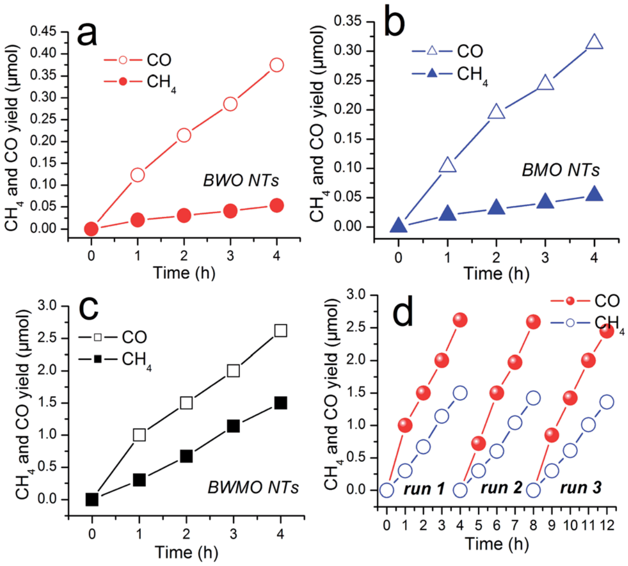

Fig. 5 Plots of CO and CH_4 production amounts as a function of visible light irradiation time over different samples: (a) BWO NTs, (b) BMO NTs and (c) BWMO NTs. (d) Stability study of photocatalytic CO and CH_4 evolution over the BWMO NTs under visible light irradiation.

μmol g^{-1} h^{-1} and 0.13 μmol g^{-1} h^{-1}), meanwhile, the pure BMO NTs also show poor CO and CH_4 production (0.80 μmol g^{-1} h^{-1} and 0.12 μmol g^{-1} h^{-1}) after irradiation for 4 h. In comparison, the BWMO NTs display more than 7 times higher activity for CO production (6.55 μmol g^{-1} h^{-1}) and CH_4 production (3.75 μmol g^{-1} h^{-1}). The highly enhanced visible-light photocatalytic activity of BWMO NTs can be ascribed to tube structure and the modified band structure, which adapt the balance between adequate redox potentials and effective visible light adsorption. Furthermore, we have tested the stability and reusability of BWMO NTs for the photocatalytic CO_2 reduction through a cycling test. As shown in Fig. 5d, the result indicates no obvious decrease of the photocatalytic activity after the three cycles, demonstrating the good stability of the BWMO NTs.

4. Conclusions

In conclusion, $Bi_2W_{0.5}Mo_{0.5}O_6$ solid solution nanotubes were used as catalyst for the CO_2 photoreduction. The BWMO NTs exhibit remarkably improved photocatalytic activities for CO_2 reduction as compared to the pure BWO NTs and BMO NTs. The photocatalytic stability of the BWMO NTs was not as satisfactory as expected and further studies are under way. This work demonstrates the promise of BWMO NTs as a photocatalyst driven by visible light for CO_2 light conversion without the addition of any noble metal assisted catalysts.

Conflicts of interest

There are no conflicts to declare.

Acknowledgements

This work was supported by the National Natural Science Foundation of China (51872068), Heilongjiang Natural Science Foundation (E2018051).

References

1 J. Mao, K. Li and T. Peng, *Catal. Sci. Technol.*, 2013, **3**, 2481–2498.

2 Y. He, L. Zhang, B. Teng and M. Fan, *Environ. Sci. Technol.*, 2014, **49**, 649–656.

3 D. Xu, B. Cheng, W. Wang, C. Jiang and J. Yu, *Appl. Catal., B*, 2018, **231**, 368–380.

4 X. Li, J. Yu, M. Jaroniec and X. Chen, *Chem. Rev.*, 2019, **119**, 3962–4179.

5 H. B. Yu, L. B. Jiang, H. Wang, B. B. Huang, X. Z. Yuan, J. H. Huang, J. Zhang and G. M. Zeng, *Small*, 2019, **15**, 1901008.

6 J. L. Liang, F. Y. Liu, J. Deng, M. Li and M. P. Tong, *Water Res.*, 2017, **123**, 632–641.

7 J. Wu, Y. Y. Sun, C. H. Gu, T. Wang, Y. J. Xin, C. Chai, C. Y. Cui and D. Ma, *Appl. Catal., B*, 2018, **237**, 622–632.

8 Q. Yan, M. Sun, T. Yan, M. M. Li, L. G. Yan, D. Wei and B. Du, *RSC Adv.*, 2015, **5**, 17245–17252.

9 A. Phuruangrat, A. Maneechote, P. Dumrongrojthanath, N. Ekthammathat, S. Thongtem and T. Thongtem, *Mater. Lett.*, 2015, **159**, 289–292.

10 Y. Zhao, X. Tan, T. Yu and S. Wang, *Mater. Lett.*, 2016, **164**, 243–247.

11 H. Huang, X. Li, J. Wang, F. Dong, P. Chu, T. Zhang and Y. Zhang, *ACS Catal.*, 2015, **5**, 4094–4103.

12 N. Tian, H. Huang, C. Liu, F. Dong, T. Zhang, X. Du, S. Yu and Y. Zhang, *J. Mater. Chem. A*, 2015, **3**, 17120–17129.

13 Y. Tian, B. Chang, J. Lu, J. Fu, F. Xi and X. Dong, *ACS Appl. Mater. Interfaces*, 2013, **5**, 7079–7085.

14 Y. Liu, Z. Zhang, Y. Fang, B. Liu, J. Huang, F. Miao, Y. Bao and B. Dong, *Appl. Catal., B*, 2019, **252**, 164–173.

15 K. Wang, Y. Zhang, L. Liu and N. Lu, *J. Mater. Sci.*, 2019, **54**, 8426–8435.

16 Y. Ma, Z. Chen, D. Qu and J. Shi, *Appl. Surf. Sci.*, 2016, **361**, 63–71.

17 F. Xu, C. Xu, H. Chen, D. Wu, Z. Gao, X. Ma, Q. Zhang and K. Jiang, *J. Alloys Compd.*, 2019, **780**, 634–642.

18 Y. Xu, J. Song, F. Chen, X. Wang, H. Yu and J. Yu, *RSC Adv.*, 2016, **6**, 65902–65910.

19 H. Zheng, P. Niu and Z. Zhao, *RSC Adv.*, 2017, **7**, 26943–26951.

20 Y. Liu, M. Zhang, L. Li and X. Zhang, *Appl. Catal., B*, 2014, **160–161**, 757–766.

21 J. Li, H. Hao and Z. Zhu, *Mater. Lett.*, 2016, **168**, 180–183.

22 Z. Li, L. Zhu, W. Wu, S. Wang and L. Qiang, *Appl. Catal., B*, 2016, **192**, 277–285.

23 F. Ma, Q. Yang, Z. Wang, Y. Liu, J. Xin, J. Zhang, Y. Hao and L. Li, *RSC Adv.*, 2018, **8**, 15853–15862.

24 M. Zhang, Y. Qi and Z. Zhang, *Polymers*, 2019, **11**, 1718.